

Carbon Deposition and Hydrocarbon Formation on Group VIII Metal Catalysts

Peter E. Nolan,[†] David C. Lynch,[‡] and Andrew Hall Cutler^{*,§}

Carbomite Company, Apache Junction, Arizona 85219, Department of Materials Science and Engineering, University of Arizona, Tucson, Arizona 85721, Minerva Laboratories, 10 Thunder Run #28C, Irvine, California 92614

Received: February 3, 1998; In Final Form: April 2, 1998

Carbon formed from CO in CO₂ at around 500 °C deposited as nanotubes and encapsulating carbons on a supported Ni catalyst without H₂ or as filaments if H₂ was present. A thermodynamic model explains how hydrogen in low concentrations controls filament morphology and why equilibrium is shifted from that for graphite during carbon deposition. Carbon deposition reaction rates at low carbon activity in the absence of hydrogen are reported. A new concept of the rate limiting step for metal-catalyzed carbon formation is proposed, where conditions inside the bulk metal are at least as important as the surface chemistry. A mechanism with an unusual type of active site can qualitatively explain carbon formation rates through a broad range of reaction conditions. When hydrogen is present, a series of hydrocarbons are believed to form, as in fuel synthesis (Fischer–Tropsch) chemistry. Surface vinyl species that have been recently shown to be intermediates in Fischer–Tropsch chemistry also may polymerize to form graphene. The formation of vinyls from CO and H via surface alkyls occurs at a greater rate than methane formation when the supply of hydrogen is limited. Hydrogen from the bulk catalyst metal (not surface adsorbed) hydrogenates the surface alkyls, indicating that hydrogen solubility may control the metal-catalyzed formation of various hydrocarbons and eventually solid graphitic carbon.

Introduction

Carbon deposition from gas precursors is important to a variety of industrial processes. Typically, carbon deposition is undesired since it deactivates catalysts. Carbon atoms on or in the catalyst significantly impact processes such as steam reforming, hydrogenation, methanation, water–gas shift, and Fischer–Tropsch fuel synthesis. Indeed, the details of carbon and hydrogen atoms' behavior lead to the mechanisms that form desirable products and undesirable byproducts or cause phenomena like metal dusting.

Carbon nanotubes and filaments are cylindrical or tubular carbon formations with radii on the nanometer scale and lengths up to several micrometers. The primary difference between a nanotube and a filament is the orientation of graphite basal planes with respect to the axis. Since the properties of graphite are anisotropic, its orientation will dictate resulting material properties such as electrical and thermal conductivity, mechanical strength, and modulus of elasticity (stiffness). Carbon encapsulation of catalyst nanoparticles can protect ferromagnetic metals from oxidation, making a promising magnetic medium. Increased understanding of the mechanisms involved in metal-catalyzed carbon formation can be used to optimize all the above processes and products. Having had the fortune of doing those few experiments necessary to see the extensive prior work of others in a unified context, we are able to write a primarily theoretical paper, in which we interpret the experimental results of others as well as include a small amount of our own data.

Catalytic production of carbon results from the decomposition of a carbon-containing gas on certain transition metals.^{1–4} The catalyst influences the structure of the carbon formed as well

as promoting reaction. The view generally held in the literature is that the carbon is formed by a solution–diffusion–precipitation process that generates graphitic (crystalline) carbon at relatively low temperatures. The graphitic deposit has been observed in various morphologies, as follows.

Filaments consist of stacked cone-segment (frustum) shaped graphite basal plane sheets and grow with a catalyst particle at their tip.^{2,5} They are illustrated using schematic cross sections in Figure 1 a,b. Hydrogen is believed to satisfy the valences at cone edges in typical filaments; and with increasing hydrogen concentration, the orientation angle between the graphite basal planes and the tube axis (θ) increases.⁶ Under certain conditions this morphological series may extend to where the basal planes are perpendicular to the cylinder axis ($\theta = 90^\circ$).⁷ Filaments with large orientation angles are often not hollow, so are more accurately described as solid cylinders.

Nanotubes are the low hydrogen end member of this series of cylindrical carbon deposits. The direction of their graphite basal planes is parallel to the tube axis ($\theta = 0^\circ$), as shown in Figure 1c. Nanotubes can be produced by catalytic carbon deposition with a catalyst particle at their tip^{8,9} and in a carbon arc without a catalyst.^{10,11} A nanotube is essentially a filament with no graphite edges, requiring no valence-satisfying species such as hydrogen. When H₂ is present in a carbon arc reactor, open-ended nanotubes can be produced with stabilized basal plane edges only at the two ends of a tube.¹²

Another graphitic nanomaterial produced by carbon deposition is encapsulated metal nanoparticles.^{13,14} These are roughly spherical formations, originally called shells, consisting of catalyst particles surrounded by graphitic carbon. They are typically found to be limited to about 30 or 40 layers of graphite basal plane (graphene) sheets, irrespective of their formation conditions or size.

[†] Carbomite Co.

[‡] University of Arizona.

[§] Minerva Laboratories.

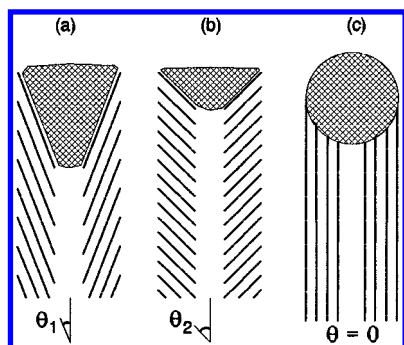


Figure 1. Schematic illustrations of (a, b) filaments and (c) a nanotube.

Encapsulated nanoparticles typically take a range of sizes, with radii from about 5 to over 100 nm. Nanotubes are more restricted in radii, typically observed with 1–3 nm inner radius and 5–20 nm outer radius. Single-wall nanotubes are found to have less than 1 to approximately 2.5 nm radii.¹⁵ Filaments may take any inner radius and range up to about 100 nm outer radius but are commonly of similar size to nanotubes. Tibbetts⁸ explains how the radii of the cylindrical structures may be controlled by equilibrium thermodynamics. We show that to be the case for the inner radius. The outer radius is often considered to be determined by the catalyst particle (for catalytically produced structures), since they usually have the same size in micrographs.⁴ That presumed causality is not supported by other evidence. Nanotubes produced by carbon arc with no catalyst particle have outer radii similar to those produced catalytically. In supported catalysts with initially small catalyst metal clusters, agglomeration takes place before typical particle sizes are reached and carbon deposition begins. When starting with a foil or large particles of catalyst metal, fragmentation occurs (and fragments are smaller than the metal's grain size). These very different processes for catalyst particle sizing produce similar filament radii, indicating a common controlling mechanism. In the present work, nanotubes tightly distributed around a 9 nm average outer radius coexisted with encapsulated particles ranging to over 40 nm radius. Thus, even when larger catalyst particles are present and undergoing carbon deposition, the nanotubes restrict themselves to the smaller radii.

All of the above morphologies were produced in the present work under similar conditions by CO disproportionation,



where C is carbon in the form of variously arranged graphene sheets. Later it will be shown that these carbon deposits are thermodynamically different from graphite. The driving force for carbon deposition by CO disproportionation is the gas-phase carbon activity (a_{C}), defined as

$$a_{\text{C}} = K_{\text{eq}} \frac{P_{\text{CO}}^2}{P_{\text{CO}_2}} \quad (2)$$

P_{CO} and P_{CO_2} are the partial pressures of CO and CO₂, and K_{eq} is the equilibrium constant for reaction 1 when the product is graphite. There are apparently two kinetic regimes as carbon activity is varied. At low carbon activity, carbon deposition rates are linearly dependent on carbon activity.¹³ At sufficiently high values of carbon activity, carbon deposition rates have little dependence on it.^{16–18}

The most elegant measurements of carbon deposition rates were done by Baker and co-workers using controlled atmosphere electron microscopy to observe filament growth.^{2,19,20} They

studied metal-catalyzed hydrocarbon decomposition and did not observe a strong dependence of carbon deposition rates or product morphologies on the gas composition. They showed that the activation energy for carbon deposition in filament form can match the activation energy of carbon diffusion through the catalyst for a variety of metals and asserted the conclusion that carbon diffusion through the catalyst particle is the rate-limiting step.²¹

There are, however, indications that carbon diffusion is not the rate-limiting step in carbon deposition under many circumstances. The activation energy of carbon diffusion through Ni might abruptly change below 700 °C,²² while the reported carbon deposition activation energy remains about the same.²³ An adsorption–diffusion isotherm for filament growth from methane on iron particles indicated that carbon diffusion through the particle was rapid compared to the preceding step of carbon formation at the top surface of the particle.²⁴ There is evidence that certain surface chemical reactions are responsible for the rate-limiting step,^{25,26} as is common in the established surface science of heterogeneous catalysis. The inability of any one proposed mechanism to explain the same phenomena over a wide range of conditions indicates that the fundamental rate-controlling mechanism is not yet understood. The purpose of the present work is to gain insight into the complex catalytic processes related to carbon deposition. Our carbon deposition results, including product morphology information, are combined with the prior work in an attempt to identify the mechanistic elements important under a wide range of conditions.

Recent results on the detailed molecular mechanism of Fischer–Tropsch catalysis²⁷ illuminate the mechanism by which filaments grow with the graphene sheets generally parallel to the catalyst particle surface and provide a dynamic mechanism for the filament structure to attain equilibrium. Certain mechanistic necessities of catalytic carbon formation may also clarify the Fischer–Tropsch mechanism.

Experimental Section

Carbon deposition rates were measured by observing weight gain during the nickel-catalyzed formation of carbon from CO. The catalyst was 70 wt % Ni on 30 wt % of a SiO₂–Al₂O₃ support (obtained from Johnson Matthey, #31276). It was exposed to CO/CO₂/N₂ mixtures with concentrations of H₂ between 0.00% and 3% and a temperature range of 745 K to 785 K. The CO/CO₂ mixture was set to give low a_{C} and avoid the conditions that would allow Ni₃C formation. Thermogravimetry was used to measure weight gain by standard methods.²⁸ Mass transport calculations and preliminary experiments were used to ensure that intrinsic chemical rates were measured and that temperature measurements were accurate. About 5 mg of catalyst in a Pt crucible was suspended in a Cahn R-100 microbalance reactor. The CO/CO₂/N₂ concentrations exiting the reactor were measured using a Shimadzu GC-8A gas chromatograph with a Alltech CTR II column to determine the reaction gas a_{C} using eq 2. For each run, the catalyst was held at 773 K for 3 h under flowing N₂ to remove moisture, then reduced in 10% H₂, 90% N₂ at 4×10^{-5} mol/s for 30 min. After flushing the reactor with N₂, the temperature for the isothermal experiment was set and reaction gas flow initiated at 6×10^{-5} mol/s.

Specimens of the material removed after a reaction experiment were examined in a Hitachi H-8100 transmission electron microscope (TEM) operating at 200 kV, to determine the morphology of deposited carbon. The graphite orientation angle

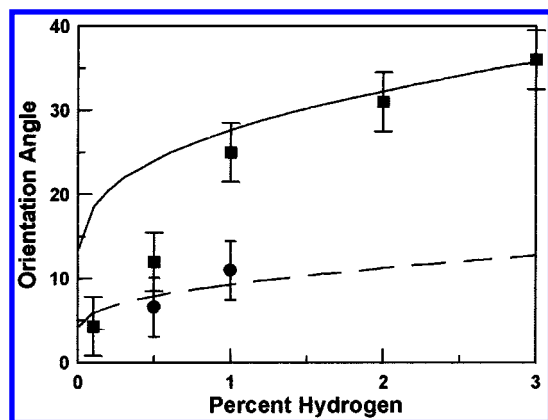


Figure 2. Measured filament orientation angle (θ) versus H_2 concentration during CO disproportionation: (■) 745 K experimental, (—) 745 K theoretical, (●) 785 K experimental, and (---) 785 K theoretical.

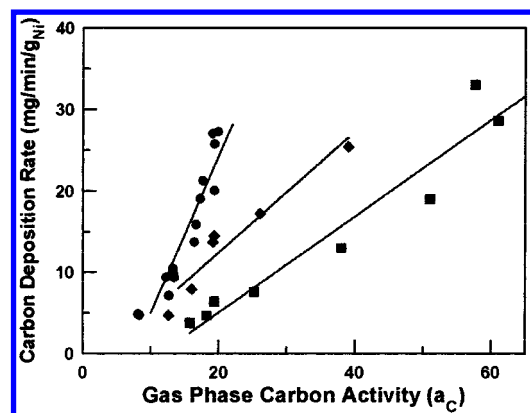


Figure 3. Maximum rates of carbon deposition on Ni/SiO₂/Al₂O₃ as a function of gas-phase carbon activity (a_c) and temperature: (■) 745 K, (◆) 765 K, and (●) 785 K.

with respect to the axis (θ) and the number of graphite basal plane edges per nanometer of tube length (E) were measured from micrographs. The parameters θ and E are geometrically related, so that

$$\sin \theta = 0.34E \quad (3)$$

since the spacing between graphite planes is constant (nominally 0.34 nm for bulk, flat graphite). Greater detail on experimental methods and the results (summarized below) are published separately.²⁹

Results

As discussed in the Introduction, different graphite morphologies were observed for the deposits formed in these experiments. Nanotubes and encapsulating shells are formed without hydrogen, and filaments are formed when hydrogen is present. There is some poorly characterized material deposited in all cases. Filament cone angle (θ) versus reaction gas H_2 concentration is shown in Figure 2 and is compared to the results of a thermodynamic model developed below.

The reaction rate data from several experiments are shown in Figures 3 and 4. Reaction rates are normalized to the mass of nickel metal in the catalyst. For individual experiments, carbon deposition weight gain curves exhibited characteristic initiation (or inception), maximum rate, and deactivation stages. These characteristic stages are common in carbon deposition studies and were directly observed by Baker and co-workers for the lengthening of individual filaments.² The relative maximum reaction rates (from the inflection point on plots of

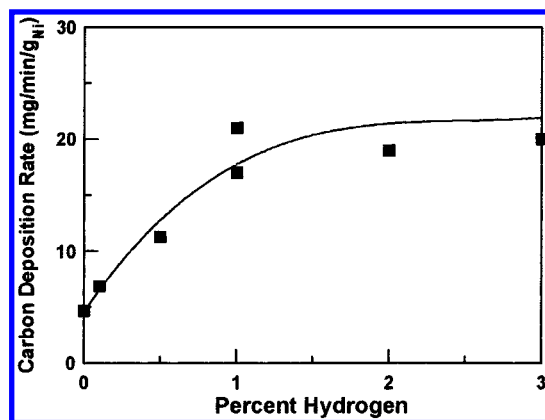


Figure 4. Maximum rates of carbon deposition on Ni/SiO₂/Al₂O₃ as a function of gas-phase H_2 concentration at 745 K, $a_c = 18$ –19.

TABLE 1: Minimum Gas-Phase Carbon Activity (a_c) and Gibbs Energy (Δg_g) for Inception of Carbon Deposition

T (K)	a_c	Δg_g (kJ/mol)
745	18	18
765	12	16
785	8	14

mass versus time) for a series of experiments are useful for kinetics analysis. Figure 3 is a plot of the maximum carbon deposition rates measured when no H_2 or N_2 was present in the CO–CO₂ gas mixture. The partial pressures of CO and CO₂ are as determined from eq 2, with a total pressure of 1 atm. Rates are plotted with respect to a_c , showing a generally linear response. The response of rates to the partial pressure of CO (or CO₂) at constant a_c (e.g., by use of diluents or a different total pressure) was not studied.

Below certain values of a_c , inception could not be achieved, and thus rates were zero. Those values of limiting a_c and the Gibbs energy ($\Delta g = RT \ln a_c$) are given in Table 1.

Figure 4 shows how the carbon deposition rate increased when small concentrations of H_2 were added to the reaction gas mixture at constant temperature. For those experiments, a_c as calculated from eq 2 was held approximately constant at 18–19.

Discussion

1. Morphological Thermodynamics of Carbon Deposits.

A thermodynamic understanding of the difference between a nanotube and a filament can be obtained by theoretical analysis. Tibbetts⁸ estimated the internal energy of a nanotube by calculating the surface energy and strain energy (of bending graphite planes) required to produce a nanotube from graphite. Other contributions can be included, such as the misalignment strain between graphite sheet layers in a nanotube³⁰ since the typical stacking sequence in flat graphite would not be maintained in the nanotube configuration. We have extended that analysis to estimate the Gibbs energy difference of a filament from graphite. The resulting model explains hydrogen's control of filament morphology, as well as literature observations that carbon deposits are in equilibrium with a substantially different gas composition than graphite is.

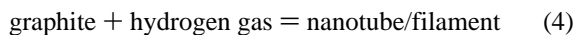
The following thermodynamic model uses standard literature values for various properties or to make estimates thereof. The small difference in Gibbs energy remaining after taking the difference of these large and unrelated numbers bears a qualitative relationship to our observations. This demonstrates a more fundamental understanding of carbon product formation than is possible through curve fitting to theoretical expressions

TABLE 2: Enthalpy and Entropy Terms (Compared to Graphite) for Cylindrical Carbon Structures

term	Δh	$T\Delta s$
1. The formation of basal plane free surfaces (bps)	$\Delta h_{\text{bps}} \cos \theta$	$T\Delta s_{\text{bps}} \cos \theta$
2. The energy of bending graphite basal planes	$\Delta h_{\text{B}} \cos \theta$	
3. Interlayer graphite stacking misalignment	$\Delta h_{\text{L}} \cos \theta$	$T\Delta s_{\text{L}} \cos \theta$
4. Formation of graphite edges with hydrogen-capped bonds	$\Delta h_{\text{E}} \sin \theta$	$T(\Delta s_{\text{E}} + \Delta s_{\text{M}}) \sin \theta$

where the shape of the curve is substantially controlled by fitted free parameters. While some of the less well constrained parameters were fitted, they were bounded by theoretical analysis, and the fitted values were found to fall inside those bounds. As all of the numbers used here have fundamental physical meanings, they could in principle be accurately derived, each by a different method, and then combined to predict our experimental results.

Consider the hypothetical reaction



to be at equilibrium, for which the Gibbs energy of reaction must be zero ($\Delta g = 0$). Then

$$\Delta h = T\Delta s \quad (5)$$

where values are molar specific to carbon (J/mol for Δh and $\text{J mol}^{-1} \text{K}^{-1}$ for Δs). Table 2 gives the terms that must be included in the enthalpy and entropy to solve eq 5. The relations and numeric values are derived assuming perfect (flaw free) graphitic structures.

For the formation of basal plane free surface (term 1), the factor of $\cos \theta$ accounts for the amount of basal plane surface exposed at the filament surface (illustrated in the Supporting Information). As θ increases, a smaller area of basal plane is exposed at the filament surface. When θ is zero, the structure is a nanotube, and the entire inside and outside surfaces are basal plane area.

To solve eq 5, it is rearranged to place the $\cos \theta$ terms on one side of the equality and $\sin \theta$ terms on the other. For the basal plane surface, $\Delta g_{\text{bps}} = \Delta h_{\text{bps}} - T\Delta s_{\text{bps}}$. Thus, when these enthalpy and entropy terms are put together in eq 5, they become $\Delta g_{\text{bps}} \cos \theta$. By definition Δg_{bps} is the surface energy of a graphite basal plane, γ_{bps} (given as 0.1 J m^{-2} in the literature), multiplied by the surface area per mole for a graphite tube,

$$\frac{2\pi(r_o + r_i)}{\nu\pi(r_o^2 - r_i^2)} = \frac{2}{\nu(r_o - r_i)} \quad (6)$$

where r_o is the tube outer radius, r_i is the tube wall inner radius, and ν is the moles per volume of graphite ($1.8 \times 10^5 \text{ mol m}^{-3}$). Thus

$$\Delta h_{\text{bps}} - T\Delta s_{\text{bps}} = \frac{2\gamma_{\text{bps}}}{\nu(r_o - r_i)} \quad (7)$$

For the energy of bending graphite basal planes (term 2), Δh_{B} is found by the method of Tibbetts.⁸ Internal energy (Δu) is determined by that method, which is approximately the same as enthalpy since $\Delta h = \Delta u + \Delta(Pv)$ and for solid carbon $\Delta(Pv)$ is negligible. The radius of curvature, R , of a tangent circle perpendicular to a cone or frustum at a point of distance r from the center line of the cone or frustum is $r \sec \theta$. Thus, the

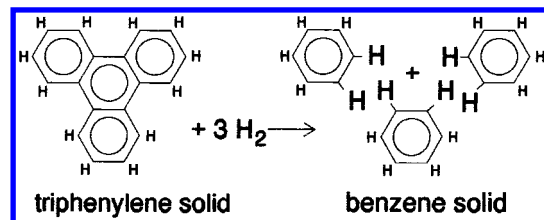


Figure 5. Illustration of reaction 9, a model for the replacement of C–C bonds with C–H bonds at graphite edges.

bending strain energy in a filament of graphene sheets per mole of carbon is

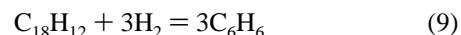
$$\Delta h_{\text{B}} = \frac{Ya^2}{12\nu(r_o^2 - r_i^2)} \int_{r_i}^{r_o} \frac{dr}{r \sec \theta} = \frac{Ya^2 \ln(r_o/r_i)}{12\nu(r_o^2 - r_i^2)} \cos \theta \quad (8)$$

where Y is Young's modulus and a is the interlayer spacing for graphite ($1 \times 10^{12} \text{ J m}^{-3}$ and 0.34 nm , respectively).

For the inner radius to be controlled by thermodynamic equilibrium, it should take the value where the strain energy of bending another inner layer exceeds the surface energy recovered by covering up the free basal plane surface of the innermost layer. Equating the enthalpy ($T = 0$) from eqs 7 and 8 for an additional layer ($r_i = r_o - 0.34 \text{ nm}$) in a nanotube predicts r_i to be 2.7 nm . That value is in good agreement with average inner radius observed in the present work of around 2.5 nm .

The value used for graphite stacking misalignment enthalpy (Δh_{L} , term 3) is estimated based on a lower limit of 1000 J/mol (the variation in half the heats of sublimation per carbon atom of polycyclic aromatics³¹) and an upper limit of 5300 J/mol (the enthalpy of turbostratic graphite³⁰). The misalignment entropy (Δs_{L}) is estimated as around $3 \text{ J mol}^{-1} \text{K}^{-1}$ based on half the average entropy of melting per carbon atom of various small solid aromatic molecules (approximating a 50–50 split between H and C). The $\cos \theta$ factor accounts for the fact that these terms are at a maximum when θ is zero, and are zero for graphite, where θ is 90° . The values used for these term 3 constants are adjusted somewhat to give a good fit to the data.

To quantify the formation of graphite edges with hydrogen-capped bonds (term 4), we used an analogous reaction:



solid triphenylene and hydrogen producing solid benzene. It is a model for the replacement of graphene C–C bonds by edge C–H bonds, illustrated in Figure 5. For reaction 9, $\Delta h_{\text{R}} = -5600 \text{ J/mol}$ and $\Delta s_{\text{R}} = -45 \text{ J mol}^{-1} \text{K}^{-1}$ (from thermodynamic tables³²) on a per mol H basis, with less than 1% variation per 100°C . These enthalpy and entropy estimates should be corrected for the effects of the different vibrational levels of the bonds, and of the restricted size of the filaments and nanotubes on the heat content of the material. Using spectroscopic data for the vibrational frequencies of the bonds and standard tables of the thermodynamic properties of the quantum simple harmonic oscillator, the correction to the enthalpy is negligible. The entropy should be corrected by 5 or $10 \text{ J mol}^{-1} \text{K}^{-1}$ for different bond vibration frequencies. A further correction to the entropy term arises from the fact that the filaments and nanotubes are of a size comparable to the wavelength of some of the phonons contributing to the heat capacity of graphite. The entropy of carbon structures of the size considered here can be estimated to be $20\text{--}30 \text{ J mol}^{-1} \text{K}^{-1}$ greater than that estimated using model compounds. While detailed calcula-

tions of these two effects are in principle possible, in themselves they would be the subject of a paper and are unlikely to be reliable enough to allow accurate results to be derived from first principles. Thus Δs_R was considered to be bounded between -20 and $-5 \text{ J mol}^{-1} \text{ K}^{-1}$ and fit as a free parameter within this range. To give these values a per mole C basis as with the other terms of Table 2, they must be multiplied by the moles of H per mole of C. That factor is determined geometrically, assuming that one hydrogen atom is taken up to satisfy valences for every two graphite edge atoms:⁶

$$\frac{\text{mol H}}{\text{mol C}} = \frac{2.1 \times 10^{-10}}{r_o - r_i} \sin \theta \quad (10)$$

which gives the $\sin \theta$ factor shown in Table 2.

In term 4 Δs_m is the entropy of mixing of the gas-phase hydrogen evaluated using the standard equation for an ideal gas ($\Delta s_m = -R \ln(P_2/P_1)$). At 1 atm total pressure and on a per mole H basis,

$$\Delta s_m = -\frac{R}{2} \ln P_{H_2} \quad (11)$$

where P_{H_2} is the partial pressure of hydrogen in the gas mixture. This result also must be multiplied by eq 10 to put it on a per mole of C basis. Note that the enthalpy of mixing for an ideal gas is zero.

Using the above terms, eq 5 becomes

$$\left(\frac{2\gamma_{\text{bps}}}{v(r_o - r_i)} + \Delta h_B + \Delta h_L - T\Delta s_L \right) \cos \theta = \frac{2.1 \times 10^{-10}}{r_o - r_i} (-\Delta h_R + T\Delta s_R - 4.2T \ln P_{H_2}) \sin \theta \quad (12)$$

which is solved for θ to give the dependence of orientation angle on H_2 concentration:

$$\theta = \tan^{-1} \left\{ \frac{\frac{2\gamma_{\text{bps}}}{v(r_o - r_i)} + \frac{Ya^2 \ln(r_o/r_i)}{12v(r_o^2 - r_i^2)} + \Delta h_L - T\Delta s_L}{\frac{2.1 \times 10^{-10}}{r_o - r_i} (-\Delta h_R + T\Delta s_R - 4.2T \ln P_{H_2})} \right\} \quad (13)$$

Typical inner and outer radii measured in the present work are 2.5 and 9 nm, respectively. These values and eq 13 are used to produce the lines shown in Figure 2. A good fit to the experimental data was achieved when setting $\Delta h_L = 1800 \text{ J/mol}$, $\Delta s_L = 3.6 \text{ J mol}^{-1} \text{ K}^{-1}$, and $\Delta s_R = -10 \text{ J mol}^{-1} \text{ K}^{-1}$, all within reasonable bounds derived from literature values. A table summarizing the values used is given in the Supporting Information.

The orientation angle is temperature dependent. Lower orientation angles are found at higher reaction temperatures (with a fixed hydrogen concentration). It is thus possible for nanotubes to be produced from a gas with a significant hydrogen concentration or fugacity (e.g., a hydrocarbon) at sufficiently high temperature, as has been reported.⁹

The Gibbs energy difference of nanotubes from graphite can be estimated based on the above modeling using the surface, bending, and misalignment energy terms while omitting the hydrogen terms. This gives

$$\Delta g_{\text{nt}} = \left(\frac{2\gamma_{\text{bps}}}{v(r_o - r_i)} + \frac{Ya^2 \ln(r_o/r_i)}{12v(r_o^2 - r_i^2)} + \Delta h_L - T\Delta s_L \right) \quad (14)$$

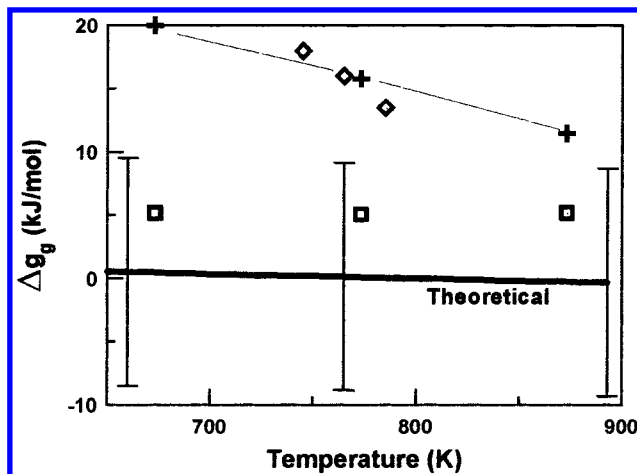


Figure 6. Gibbs energy differences (Δg_g) required to form carbon structures: (+) for CO disproportionation,²⁶ (□) for CH_4 decomposition,²⁶ (◇) from inception time for CO disproportionation (present work), and (—) theoretical (eq 14, present work).

Equation 14 may be used to estimate the enthalpy of formation of a nanotube, by setting T to zero. The resulting value can be compared to what Setton derived using a (6, 12) Lennard-Jones formulation.³³ Setton calculated enthalpy values of 6.9–8.7 kJ/mol for a nanotube with $r_o = 3.2 \text{ nm}$ and $r_i = 1.7 \text{ nm}$. The present method gives an enthalpy of 7.2 kJ/mol with those radii (and the same values for constants as used above). The equation also gives the temperature at which nanotubes are preferred to graphite ($\Delta g_{\text{nt}} < 0$); this is where nanotubes are the equilibrium form of carbon. For the typical radii measured in the present work, that temperature is about 800 K, appropriate for the reaction temperatures used. For the radii given above from Setton, that temperature is 2000 K, appropriate for conditions in the carbon arc.

When the different geometry is accounted for, the Gibbs energy difference from graphite for spherical encapsulates can be estimated as well. The expression is

$$\Delta g_{\text{encap.}} = \frac{3(r_o^2 + r_i^2)\gamma_{\text{bps}}}{v(r_o^3 - r_i^3)} + \frac{\pi Ya^2(r_o + r_i) \ln(r_o/r_i)}{16v(r_o^3 - r_i^3)} + \Delta h_L - T\Delta s_L \quad (15)$$

Equations 14 and 15 imply that nanotubes have smaller radii than the encapsulates they are in equilibrium with. TEM observations show that encapsulates have larger radii than nanotubes in any given experiment.

There have been several reports of measured Gibbs energy differences from graphite required before carbon deposition can occur.²⁶ The term Δg_g will be used to refer to the Gibbs energy difference between a given carbon product and standard-state graphite. The values in the literature were found by measuring the gas mixture at equilibrium when shifting between carbon deposition and carbon gasification and comparing this composition to the mixture that would be predicted using standard graphite equilibrium data.

Data for hydrogen-free CO-derived deposits can be compared to results obtained by us using an entirely different approach. We considered the inception time at different gas compositions. Those measurements were used to determine the value of a_C (or Δg_g) at which inception no longer occurs in finite time. The results (Table 1) are plotted, along with the literature results, in Figure 6. There is reasonable agreement between the two methods of determining the Δg_g for carbon deposited by CO

disproportionation. These Δg_g values are larger than those reported for methane decomposition (also shown in Figure 6), since hydrogen available in the methane system satisfies point defects and opens the orientation angle to give a lower enthalpy product. Increasing Δg_g values for CO disproportionation at lower temperatures would also be due to an expected increase in defects at lower temperatures. See the Supporting Information for a discussion of point defects.

Figure 6 also shows the Δg_g for nanotubes calculated using eq 14. We expect the theoretical curve for nanotubes (no point defects) and the experimental values for methane decomposition derived filaments (with satisfied point defects) to have similar magnitudes of Δg_g . Uncertainty in the standard thermodynamic data for graphite is believed to be 9 kJ/mol.²⁶ The greatest source of error in the theoretical curve is from that uncertainty in the Gibbs energy of graphite. Thus, error bars were placed on the theoretical curve shown in Figure 6, showing that the theoretical and the methane decomposition curves are indistinguishable.

2. The Role of Hydrogen in Carbon Deposition. Hydrogen has several well-known roles in carbon deposition. It is believed to contribute to catalyst particle fragmentation, prevent carbide formation, and control properties of the catalyst by lattice restructuring. The relevance of hydrogen to filament orientation angle has only recently been recognized.⁶ In the more simplified experiments of the present work, the impact of hydrogen on graphite edge formation was isolated as much as possible from the other effects of hydrogen.

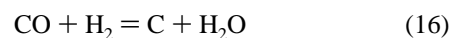
The impact of hydrogen on filament morphology clarifies some details of the diffusion–precipitation mechanism. Free valences (or dangling bonds) are excessively energetic and cannot actually exist, even for an instant, at the edge of growing graphite planes under conditions less energetic than the carbon arc. During precipitation, something must cap the free valences at the edge of the graphite sheet to which new carbons will add. Without hydrogen, this means that the sp^2 -hybridized carbon orbitals in graphite, and hence the basal planes, must point at the catalyst surface (the graphene sheet must be perpendicular to it). Hydrogen can cap valences and allow free plane edges to be left behind. It can also bond to the edges to form sp^3 -hybridized carbons so that the “free” carbon valences needed for plane growth can be stabilized by the catalyst surface while the graphite basal plane lies parallel to it. Plane formation then occurs by interconversion of the various C–H moieties at the plane edge as carbon atoms are added to it, a process that would also be catalyzed by the metals that catalyze filament growth.

Using this knowledge of how carbon precipitates from the catalyst surface, we can explain the shapes of the catalyst particles shown in the literature associated with tubular carbon products. Two commonly seen catalyst particle shapes³⁴ that are clearly different from each other are pear-shaped (roughly conical) and spherical. The conical particles are found at the tip of filaments,³⁵ and nearly spherical particles³⁶ are observed at the tip of nanotubes. That fits the concept that filament formation, with the aid of hydrogen, entails carbon precipitation generally parallel to the catalyst surface. The carbon takes the shape of stacked cones precipitating one at a time from the particle, determining the shape of the bottom of the particle.

Nanotubes must precipitate from the catalyst generally perpendicular to its surface in order to satisfy plane edge valences by bonding to the catalyst particle surface. Accordingly, the basal planes do not form in the shape of the particle,

but are the shape of a cross section of the particle. Thus cylindrical nanotubes with a circular cross section are produced by spherical particles with a circular cross section. The consequence of this, and the thermodynamics control shown in section 1 above, belies the commonly held belief that the catalyst particle determines the product size. It is more likely the opposite. The thermodynamics of the carbon deposition system determines the size and structure of the carbons formed, and thus the size and shape of the catalyst particle. Crystallographic considerations such as preferred planes for reaction and precipitation⁵ play a role, but do not solely determine the particle shape.

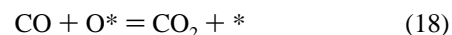
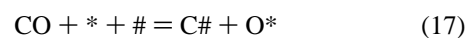
3. Carbon Deposition Mechanisms. Reaction rate data for CO disproportionation on a supported catalyst in the complete absence of hydrogen are reported here. In prior literature where reaction rates were measured, hydrogen was typically present as an impurity. The H_2 impurity was either known to exist³ or not reported but apparent since filaments were produced.²³ Although often not found to be the case,^{1,37} there can be significant carbon deposition rates without hydrogen present, as shown in Figure 3. Without hydrogen, carbon can only be formed from CO by disproportionation (reaction 1). When H_2 is added to the reaction gas, carbon may also form by the overall reaction of CO hydrogenation,



which can be considered responsible for the increasing carbon deposition rate shown in Figure 4.^{1,38}

Based on the literature, the rate and mechanism involved in carbon deposition appear to depend on the reaction conditions. Reaction conditions include temperature, reactant partial pressures, particularly carbon activity (e.g., low a_C from a CO/ CO_2 mixture high in CO_2 or high carbon activity from pure CO or a hydrocarbon), hydrogen concentration (or fugacity for the case of hydrocarbons), and the catalyst itself (e.g., the support used or the catalyst metal alloyed with another metal). In the following, an attempt is made to generate a single model operative for most of the above conditions.

The general trend of reaction rate response to the above conditions may be found by foregoing a common assumption of heterogeneous catalysis. Instead of only one type of active site on the surface of the catalyst, we assume that there are two different types of active site: possibly a surface site and a subsurface site. Then the reaction path for CO disproportionation can be generalized as having the following steps:



where * and # designate the two types of sites, and \underline{C} represents carbon in solution in the catalyst metal. The # active site might be where individual carbon atoms form and dissolve into the bulk catalyst metal. Rate limitation and catalyst deactivation may result from slow removal of carbon atoms from these sites. Step 17 incorporates what are probably several complicated steps, but which are considered to be near equilibrium. Taking step 19 as the rate-limiting step (all other steps being near equilibrium), the rate equation for this

mechanism can be derived (shown in the Supporting Information). The result is

$$\text{rate} = kK_3 \frac{a_C \#_T}{1 + K_3 a_C} \quad (20)$$

where k is the temperature-dependent rate constant, K_3 is a combination of rate constants, and $\#_T$ is the total of occupied and unoccupied sites of the second type.

To be correct, a_C in eq 20 should be replaced by a different activity, a'_C . This new term a'_C is the gas-phase carbon activity relative to the type of carbon being formed, rather than to graphite. The difference between a'_C and a_C results from the difference in Gibbs energy (Figure 6) between the actual carbon products formed and graphite, such that (for CO disproportionation)

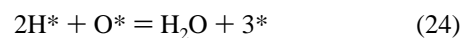
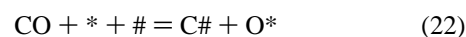
$$a'_C = a_C e^{\Delta g_g/RT} \quad (21)$$

The trends that eq 20 predict are consistent with the literature. It gives a rate that is linear in a'_C for small values of a'_C and approximately constant (at a given $\#_T$) for large values of a'_C . As the thermodynamic properties of the carbon formed are not generally known, a_C is generally calculated instead of a'_C . Under reasonable conditions a_C will be proportional to a'_C for a given set of experiments, with a proportionality constant typically between 2 and 25. To most closely model the data, the relation of a'_C to a_C must be accurately known for each particular experiment. That information is not generally reported in or derivable from the literature.

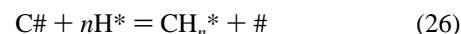
Control of reaction rate by the second type of active site can account for other literature findings. Similarity of the apparent activation energy of filament growth to that of carbon diffusion in the catalyst metal could be due to the mobility of carbon from subsurface sites, a mechanism potentially similar to diffusion. The finding that significant rate increases result from alloying a catalyst with a noncatalytic metal could be explained by the ability of surface clusters to increase $\#_T$ and thus rate. Also, carbon on the second type of sites might be compared to the surface carbide as discussed by Alstrup²⁵ that controls the carbon activity gradient through the catalyst particle. The inception/deactivation property common to carbon deposition could be attributed to $\#_T$ variation during the experiment. That variation could be caused first by low carbon presence creating sites, then by high carbon coverage blocking sites. Determination of $\#_T$ would probably not be as easy as measurement of surface adsorption sites (i.e., $\#_T$). There is no reason to expect that the response of $\#$ sites to gas adsorption compares to that of typical surface active sites.

The general form of eq 20 can describe the known trends in carbon deposition from CO at low a_C , and can be applied to hydrocarbon decomposition with very high carbon activity. In other than CO disproportionation, a_C as defined by eq 2 is replaced by an appropriate determination of carbon activity for the particular system. The simplicity of eq 20 disguises the underlying broad complexity of this system. For instance, the $\#_T$ term is probably strongly dependent on a number of parameters. The above rate law is the simplest hypothesis consistent with the literature. Given the lack of information needed to determine Δg_g , it is difficult to test this hypothesis in greater detail. The principal weakness of the above formulation is its inability to predict the effect of the partial pressure of CO (at constant a_C) that has been observed.²⁶

The effect of hydrogen on the above proposed mechanism may be examined by considering the following reaction steps:



The rate equation for this mechanism (with reaction 25 as the rate-limiting step) is similar to eq 20, except that the carbon activity (a'_C equivalent) is calculated from reaction 16 instead of reaction 1. Unfortunately, to ascertain the carbon activity associated with reaction 16, it would be necessary to measure $P_{\text{H}_2\text{O}}$ on the catalyst surface, which is extremely difficult. In principle, some combination of the two rates would account for the increasing total reaction rate (for low H_2 concentrations). At high concentrations of H_2 , adsorbed hydrogen competes with and "crowds out" the adsorption of CO ,²⁵ at which point the above assumptions would no longer apply. The literature findings that a surface chemistry step is rate limiting under some conditions argue against the assumption that step 19 (or step 25) is limiting. The additional complexities introduced by the presence of hydrogen call for a more detailed analysis. Other steps involving hydrocarbon intermediates, of the form



where n is 1 through 3, are considered in section 4 below.

The overall rate law for CO consumption during carbon deposition from CO and H_2 might then take a form such as $k_1 P_{\text{CO}}^2 + k_2 P_{\text{CO}} P_{\text{H}_2}$. By analogy to the prior literature and the above, the first term is likely a complex expression that reduces to a dependence on P_{CO}^2 at very low pressure (such that CO_2 presence is negligible) and to carbon activity at higher pressures. The second term in this rate law is important when there is a high hydrogen concentration. A large fraction of the surface carbon would be present as methyl ($-\text{CH}_3$), and the rate-limiting step becomes obtaining carbon from CO.

4. Application to Fischer–Tropsch Catalysis. Fischer–Tropsch (FT) catalysis is the reaction of CO and H_2 at low temperatures (e.g., 300 °C) to form hydrocarbons such as liquid motor fuel. When considered in light of the present results, the work of Maitlis and co-workers²⁷ on FT catalysis leads to a mechanistic understanding of the entire spectrum of catalysis by transition metals. In addition, the work of Vannice³⁹ and of Johnson and co-workers⁴⁰ can be used to clarify and confirm certain important mechanistic details.

Methyl ($-\text{CH}_3$) adsorbed on Ni has been shown to not react with surface-bound hydrogen.⁴⁰ It only reacts with hydrogen dissolved in the Ni bulk phase. An illustration of methyl and other surface species discussed here is given in the Supporting Information.

Carbon as well as hydrogen dissolves in the typical FT catalyst metals. Thus it is possible that the source of the observed C_2 product (C_2H_n) is reaction of surface methyl with dissolved carbon analogous to the reaction of surface methyl with dissolved hydrogen. Methyl, methylene, and methyne are all known to adsorb at the same surface site, nestled in the hollow between three adjacent metal atoms.⁴¹ It is reasonable to assume that higher alkyl species will bind in the same manner to the same site (which is known to be true for ethylidyne). Thus the addition of bulk dissolved carbon to produce ethylidyne

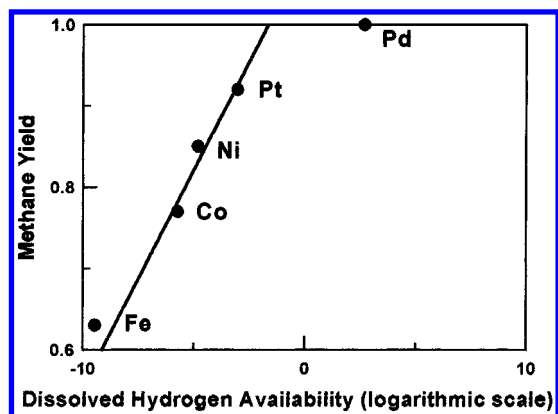


Figure 7. The molar methane yield from Vannice,³⁹ for H_2/CO ratio of 1.6, versus metal-dissolved hydrogen availability estimated as $\ln(H \text{ solubility} \times N_{CO}^{-3/2})$.

(methyl methyne) occurs with the initial methyl bound to its equilibrium adsorption site and produces ethylidyne already bound to its equilibrium surface adsorption site. This could also be the source of the vinyl that initiates further FT synthesis.

Considering the above, we believe that the branching of products to methane (CH_4) or higher hydrocarbons (or the chain termination probability for the higher hydrocarbons) is controlled by the amount of hydrogen dissolved in the metal. The more hydrogen available in solution, the more rapidly it adds to surface methyl to form methane. Initially formed surface-bound methyl will be hydrogenated before it can start down the FT chemistry path. When dissolved hydrogen available to surface species is limited, higher hydrocarbons have an opportunity to form. Figure 7 gives the response of methane yield (as determined by Vannice³⁹ for the group VIII metals) to the estimated availability of bulk-dissolved hydrogen at active sites. Methane production is shown to increase with dissolved hydrogen availability. The availability to an active site of hydrogen dissolved in the catalyst metal is estimated as the natural log of hydrogen solubility in the metal (atoms per volume) times the diffusion volume. Hydrogen solubility values used for Fe, Pt, Pd⁴² and Co, Ni⁴³ are those for the temperature at which the Vannice catalytic reaction data were taken. Diffusion volume is the cube of diffusion distance, which is proportional to the square root of the residence time. Residence time is the inverse of turnover number, N_{CO} , given by Vannice.³⁹ Thus we take the estimated dissolved hydrogen availability to an active site as $\ln(H \text{ solubility} \times N_{CO}^{-3/2})$.

Palladium has an exceptionally high hydrogen solubility (2.2 at. % compared to 5×10^{-4} to 10^{-8} % for the other group VIII metals at 300 °C), and methane is the only product observed from Pd under FT conditions.³⁹ As seen in Figure 7, the hydrogen availability in Pd is well above the level predicted to lead to 100% methanation. Also, Ru (normally a FT catalyst with a good yield of C_2^+) becomes selective for methane as CO is reduced to trace levels, where dissolved carbon falls as P_{CO} , but dissolved hydrogen falls more slowly, as $P_{H_2}^{1/2}$. This gives a theoretical explanation for the industrial practice of running FT plants at high total pressure, since C_2^+ yield increases as P_{CO} and methane yield increases only as $P_{H_2}^{1/2}$.⁴⁴

Khassin and co-workers⁴⁵ observe that, under constant reaction conditions, the chain termination probability depends on particle size for Co catalysts in the same way that hydrogen solubility depends on Co particle size. This again implies that methane formation and chain termination occur when a dissolved hydrogen atom reacts with an adsorbed surface species.

Tavares and co-workers⁴⁶ show that the addition of Cu to Ni catalysts greatly reduces the rate of carbon deposition from $CO-H_2$ mixtures without significantly changing the rate of methanation. That is as expected, since hydrogen solubility in Cu–Ni alloys is not dependent on composition for Ni-rich alloys.⁴⁷ Also, the methanation rates given for constant CO partial pressures fit well to $P_{H_2}^{1/2}$. Carbon is far less soluble in Cu than Ni, and solubility varies smoothly with composition. The observation that carbon deposition rates fell as Cu was added is consistent with the need for carbon to dissolve in the catalyst before depositing. That Cu is not effective as an FT catalyst, unlike metals such as Ni, Co, and Fe, in which carbon is much more soluble, implies a role for bulk-dissolved carbon in forming polymerization active surface species that lead to FT products rather than methane.

Maitlis and co-workers²⁷ show in model compounds that carbon is preferentially incorporated into hydrocarbons from methylene, not methyl. The metal must have reasonable amounts of methylene in equilibrium with methyl on the surface in order to be active as a FT or carbonization catalyst. In support of this, Alstrup and Tavares⁴⁸ argue that during deposition of carbon from methane on Fe and Ni, the conversion of surface methyl to surface methylene is rate limiting. The role of promoters and alloying additions may be to control the relative ratios of methylene and methyl. Zaera⁴⁹ discusses the chemistry of surface bound C_1H_n 's ($1 \leq n \leq 3$) and shows that they are all close in energy and interconvert readily.

Orbital symmetry requirements (the Woodward–Hoffmann rules) have been analyzed for the reaction of two metal–carbon σ bonds to form a C–C bond.⁵⁰ This “2+2” reaction is not allowed for carbon or hydrogen atoms bonded to different metal atoms. However, the reaction is allowed, and often observed, for carbon or hydrogen atoms when both are bonded to the same metal atom (in which case it is a reductive elimination).

Presumably, on a metal surface, forward and reverse reductive elimination (a 2+2 reaction) is symmetry allowed as long as the surface-bound species are able to come close enough that they are both bound to one common metal atom. The 2+2 reactions are symmetry forbidden if the two surface-bound species cannot come close enough to share a common metal atom. See the Supporting Material for further details.

Methyl and hydrogen can be bonded to the same metal atom if a dissolved hydrogen atom occupies the interstitial site directly below the 3-fold surface site occupied by the methyl. Adsorption or desorption of methane thus requires enough activation energy to move the hydrogen atom from the interstitial site to the surface, as well as to cause reaction (i.e., enthalpy terms from dissolution, diffusion, and CH_n interconversion). Carbon also dissolves interstitially in metals and could thus bond to the same metal atom as a surface CH_n . Reductive elimination would then form a C_2H_n surface moiety that could rearrange to vinyl and take part in FT chemistry.

The product stereochemistry and competitive branching ratios reported by Maitlis and co-workers²⁷ are consistent with orbital symmetry control of reaction between carbon species bonded to two different metal atoms. The addition of a saturated alkyl group to methylene and the insertion of methyl into the sp^2 carbon to metal σ bond of a surface-bound vinyl group are both forbidden on orbital symmetry grounds.

The addition of vinyl to methylene to form a tridentate allyl product is an allowed reaction. This is illustrated for a metal surface in the Supporting Information. A 1,3 hydrogen shift to regenerate surface-bound vinyl is also symmetry allowed. Mass spectral data kindly provided by Maitlis do not appear consistent

with a tridentate allylic intermediate. Some transition state in which methylene addition to vinyl and a 1,3 hydrogen shift occur at the same time is necessary, since the chain termination probability in FT synthesis stays roughly constant over two broad ranges of carbon number. If the metal surface is a catalyst for isomerization of a metal-2-ene intermediate to metal-1-ene, which could then add another methylene, then the 3-ene, 4-ene, etc., species should also form. These could not add methylene. A longer chain would have more positions for the double bond, which would spend proportionately less time at position 1, bound to the metal surface. It is only this surface-bound 1-alkene that can add a further methylene group and extend the carbon chain. Thus, if the double bond could be isomerized, it is reasonable to expect that chains would grow more slowly as they become longer, and the chain growth probability would decrease as carbon number increased (since there is no reason to expect the rate of chain termination to depend on length). However, the chain growth probability is observed to maintain a constant value over a wide range of carbon numbers, so we do not believe that a monodentate allylic intermediate forms and later isomerizes.

The orbital symmetry constraint does not directly require that an sp^2 carbon rather than an sp^3 carbon add to methylene. It simply requires that the carbon adding also be part of a C—C π bond that participates in the reaction in a concerted manner, and an sp^3 carbon cannot also be part of a π -bonded system.

The difficulty of decomposing phenyl model compounds²⁷ (similar to that for methyl compounds) is presumably because the double bond of the vinyl moiety is involved in the reaction—as required by orbital symmetry considerations—and thus the aromatic character of the benzene ring is temporarily lost in the activated complex. Thus, much more activation energy would be required to cause methylene addition at a reasonable rate or, alternatively, to activate energetic multistep processes that lead to “forbidden” products.

The presumption of orbital symmetry control also leads to the correct conclusion that group Ib and IIb elements should be catalytically inactive for FT synthesis. Symmetry requirements for all of the candidate reactions require that two different d orbitals on a single metal atom participate in the reaction, something not possible with d^9 or d^{10} metals.

Thus we hypothesize that chain growth starts with the formation of ethylidyne by addition of dissolved carbon to surface methyl. This ethylidyne then isomerizes to vinyl. Chain growth continues by concerted addition of surface-bound methylene to surface-bound alk-1-ene_n to form surface-bound alk-1-ene_{n+1}. Growth is terminated by addition of metal bulk dissolved hydrogen to the metal—carbon σ bond.

This mechanism does not explain the relative lack of C_2 versus C_3 product normally found in FT synthesis. Addition of various sources of vinyl was found to dramatically increase C_2 yield to well above C_3 yield.⁵¹ Yet at higher carbon numbers (C_5^+), there was still an Anderson—Schultz—Flory product distribution consistent with constant chain propagation (or termination) probability. To explain the lack of C_2 product in typical FT synthesis would require methylene to react with some rearrangement product of ethylidyne before it can isomerize to vinyl.

In the surface science literature ethylidyne is observed to form under vacuum conditions from vinyl iodide on various metals.⁵² Under these conditions, ethylidyne is believed to form through a vinyl intermediate regardless of the precursor.⁵³ For ethylidyne layers with coadsorbed H and CO in equilibrium with gas-phase H_2 and CO at elevated pressures, the ethylidyne was

stabilized against decomposition or reaction to form certain intermediates.⁵⁴ Typical surface science conditions are equivalent to about 1 part in 10^9 H_2 at atmospheric pressure. Dehydrogenation is strongly favored, and carbon is the expected product. Under FT conditions the equilibrium is reversed as there is much more hydrogen. Thus ethylidyne should be the precursor to vinyl under FT conditions instead of the product of vinyl decomposition as it is under vacuum. For the typical FT yield minimum at C_2 , we assume that ethylidyne or some intermediate on its route to vinyl can react with some surface CH_n and form a C_3 product that is a FT polymerization intermediate. This unknown reaction must involve both carbons of the ethylidyne, or methyne would also undergo it and there would be no dip at C_2 .

The mechanism hypothesized above explains why FT products are formed at high relative values of hydrogen fugacity to a_C (e.g., 275 °C, $H_2/CO = 2$) while carbon filaments or nanotubes with equilibrium controlled morphology are formed over similar catalysts at low relative ratio of hydrogen fugacity to a_C (e.g., our experimental conditions, or 90% H_2 , 10% CH_4 at 1050 °C). All of the surface-bound C_1H_n ($1 \leq n \leq 3$) species are in equilibrium on the surface.⁴⁹ If products heavier than methane are to form, hydrogen availability must be restricted so that reasonable concentrations of methyne and methylene exist to react with vinyl (discussed in the Supporting Information).

At low hydrogen fugacity, multidentate hydrocarbons will add carbon from the metal phase, forming additional growth centers, and react with themselves to form polycyclic structures. These surface hydrocarbon islands can reach equilibrium through repeated addition and loss of hydrogen and carbon atoms dissolved in the metal catalyst. This dynamic process allows the frusta in filaments—for example, $C_{30,000}H_{400}$ molecules—to achieve the exact shape that allows them to stack into the filament structure and have an angle θ determined by the equilibrium availability of hydrogen.

Nanotube growth in the absence of hydrogen occurs by the addition of carbon atoms diffusing through the catalyst metal to the growing edges of aromatic graphene sheets. With hydrogen present, the edge carbons in the growing graphene sheet can be hydrogenated to a tetrahedral sp^3 state so that the free valences can point down and bind to the metal surface while the graphene sheet lies parallel to it. Details of aromatization are discussed in the Supporting Information.

5. Kinetics of Heterogeneous C—H Reactions. Without hydrogen, nanotubes grow edge-on to the catalyst metal surface and clearly must grow by solution and diffusion of carbon atoms through the bulk metal. There are no methylenes to add onto the carbon since no hydrogen is present. Kinetics derived from this model is discussed in section 3 above. With hydrogen, in the limiting case of methanation, carbon is a surface species and C_2^+ products cannot form from CH_n — CH_n surface reactions. In Fischer—Tropsch catalysis, carbon is present in surface species, and chain growth occurs by carbon moieties finding each other through surface diffusion. We believe that the C_2 initiator for chain growth is formed by reaction of surface methyl with a bulk-dissolved carbon atom. If this is so, then the rate of forming surface C_2 , and hence the branching between methanation and FT products, is also directly related to solution of carbon atoms into the bulk metal.

As hydrogen becomes less available than in FT chemistry, the chain growth probability becomes unity, and the hydrocarbons will lose hydrogen back to the metal until they become graphene. Diffusion of hydrogen through metals is much faster

than that of carbon (the ratio of their diffusion constants in Ni at 500 °C is about 3×10^6). Hydrogen concentration or activity gradients are unlikely in a catalyst particle. Adequate hydrogen should be available at the carbon to metal particle interface to form whatever hydrocarbon moieties are sterically or mechanistically required at this interface. Under various conditions hydrocarbon surface species are abundant and have much higher mobility than carbon does through the bulk metal. Thus in filaments there may be regimes where carbon is delivered to the growing edge by diffusion of surface species, and the filament is filled in by bulk carbon diffusion through the catalyst. Meanwhile the uniform hydrogen concentration in the catalyst particle facilitates restructuring and annealing of the growing carbon layers.

Conclusion

Theoretically derived approximate thermodynamic expressions for the relationship between filament cone angle and hydrogen partial pressure, for the Gibbs energy of carbon formations, and for the inner radius of nanotubes match experimental results reasonably well. They show that the morphologies of carbon deposits are largely equilibrium controlled. This increased understanding allows control of deposit morphology and, hence, properties. Materials properties might be tailored by controlling the hydrogen concentration when making filaments and nanotubes catalytically, so as to control the orientation of graphite basal planes.

The kinetics of carbon deposition are very complex. By assuming that there is a second type of *subsurface* active site involved in the mechanisms of carbon formation, it is possible to obtain a simplified rate expression that is useful over a broad range of reaction conditions for carbon deposition. This subsurface active site may also be relevant to the formation rate of C_2^+ hydrocarbons in Fischer–Tropsch synthesis.

The same fundamental chemistry occurring on and inside metal catalyst particles governs the production of carbon deposits (filaments, nanotubes, and encapsulates) and methane or higher hydrocarbons (FT synthesis products). Carbon and hydrogen atoms in solid solution in the catalyst metal particles are important in all of these processes, controlling the observed rates and product yields or structure of deposits.

With hydrogen present, carbon deposits form through Fischer–Tropsch catalysis. During the inception period of carbon deposition, FT chemistry creates large enough carbon islands on the catalyst surface to constrain later reaction intermediates and efficiently convert them to graphene sheets. Without hydrogen the only FT chemistry possible is the addition of carbon atoms dissolved in the catalyst to surface-bound species, in this case graphene sheets, to form products such as nanotubes.

Combining diverse results reveals that FT chemistry (and catalytic carbon deposition) is controlled by the solubilities of hydrogen and carbon atoms in the catalyst metal. Metals with a high solubility of hydrogen relative to carbon are methanation catalysts. Higher hydrocarbons may only form after a dissolved carbon atom adds to a surface carbon species to form a polymerization active group. Chain extension occurs by addition of surface species, while chain termination occurs by reaction with a hydrogen atom dissolved in the catalyst metal.

Acknowledgment. The authors would like to thank Peter Maitlis for his valuable comments and for sharing unpublished data with us. We also thank Jun Jiao, Kristen Law, Michael Schabel, Supapan Seraphin, George Henschke, and Josie Tanner

for their assistance, and Ib Alstrup for helpful observations. Support was provided by Minerva Laboratories, Carbomite Company, and in part by the NASA/UA Space Engineering Research Center.

References and Notes

- (1) Walker, P. L.; Rakszawski, J. F.; Imperial, G. R. *J. Phys. Chem.* **1959**, *63*, 133–149.
- (2) Baker, R. T. K.; Harris, P. S. The Formation of Filamentous Carbon. In *Chemistry and Physics of Carbon*; Walker, P. L., Thrower, P. A., Eds.; Marcel Dekker: New York, 1978; Vol. 14, pp 83–165.
- (3) Jablonski, G. A.; Geurts, F. W.; Sacco, A.; Biederman, R. R. *Carbon* **1992**, *30*, 87–98.
- (4) Rodriguez, N. M. *J. Mater. Res.* **1993**, *8*, 3233–3250.
- (5) Yang, R. T.; Chen, L. P. *J. Catal.* **1989**, *115*, 52–64.
- (6) Nolan, P. E.; Schabel, M. J.; Lynch, D. C.; Cutler, A. H. *Carbon* **1995**, *33*, 79–85.
- (7) Murayama, H.; Maeda, T. *Nature* **1990**, *345*, 791–793.
- (8) Tibbetts, G. G. *J. Cryst. Growth* **1984**, *66*, 632.
- (9) Ivanov, V.; Nagy, J. B.; Lambin, P.; Lucas, A.; Zhang, X. B.; Zhang, X. F.; Bernaerts, D.; Van Tendeloo, G.; Amelinckx, S.; Van Landuyt, J. *Chem. Phys. Lett.* **1994**, *223*, 329–335.
- (10) Bacon, R. *J. Appl. Phys.* **1960**, *31*, 283–290.
- (11) Iijima, S. *Nature* **1991**, *354*, 56–58.
- (12) Wang, X.; Lin, X.; Mesle, M.; Jarrold, M.; Dravid, V.; Ketterson, J.; Chang, R. *J. Mater. Res.* **1995**, *10*, 1977–1983.
- (13) Audier, M.; Coulon, M. *Carbon* **1985**, *23*, 3 (3), 317.
- (14) Nolan, P. E.; Lynch, D. C.; Cutler, A. H. *Carbon* **1994**, *32*, 479.
- (15) Dai, H.; Rinzler, A. G.; Nikolaev, P.; Andreas, T.; Colbert, D. T.; Smalley, R. E. *Chem. Phys. Lett.* **1996**, *260*, 471–475.
- (16) Bianchini, E. C.; Lund, C. R. F. *J. Catal.* **1989**, *117*, 455.
- (17) Safvi, S. A.; Bianchini, E. C.; Lund, C. R. F. *Carbon* **1991**, *29*, 1245–1250.
- (18) Holstein, W. L. *J. Catal.* **1995**, *152*, 42–51.
- (19) Baker, R. T. K.; Barber, M. A.; Harris, F. S.; Feates, F. S.; Waite, R. J. *J. Catal.* **1972**, *26*, 51.
- (20) Baker, R. T. K.; Harris, P. S.; Thomas, R. B.; Waite, R. J. *J. Catal.* **1973**, *30*, 86.
- (21) Baker, R. T. K. *Carbon* **1989**, *27*, 315.
- (22) Massaro, T. A.; Petersen, T. M. *J. Appl. Phys.* **1971**, *42*, 5534–5539.
- (23) Tottrup, P. B. *J. Catal.* **1976**, *42*, 29–36.
- (24) Tibbetts, G. G.; Devour, M. G.; Rodda, E. J. *Carbon* **1987**, *25*, 5(3), 367.
- (25) Alstrup, I. *J. Catal.* **1988**, *109*, 241.
- (26) Tavares, M. T.; Alstrup, I.; Bernardo, C. A.; Rostrup-Nielsen, J. R. *J. Catal.* **1994**, *147*, 525.
- (27) Maitlis, P. M.; Long, H. C.; Quyoum, R.; Turner, M. L.; Wang, Z. Q. *Chem. Commun.* **1996**, 1.
- (28) Speyer, R. F. *Thermal Analysis of Materials*; Marcel Dekker: New York, 1994.
- (29) Nolan, P. E. Hydrogen Control of Catalytic Carbon Deposition. Dissertation, The University of Arizona, 1995.
- (30) Speck, J. S.; Endo, M.; Dresslehaus, M. S. *J. Cryst. Growth* **1989**, *94*, 834–848.
- (31) *Lange's Handbook of Chemistry*, 14th ed.; Dean, J. A., Ed.; McGraw-Hill: New York, 1992.
- (32) Rouine, A. HSC Software version 3.31; Outokumpu Research Center: Pori, Finland, 1989.
- (33) Setton, R. *Carbon* **1996**, *34*, 69.
- (34) Chitrapu, P.; Lund, C. R. F.; Tsamopoulos, J. A. *Carbon* **1992**, *30*, 285–293.
- (35) Audier, M.; Coulon, M.; Oberlin, A. *Carbon* **1980**, *18*, 73–76.
- (36) Oberlin, A.; Endo, M.; Koyama, T. *J. Cryst. Growth* **1976**, *32*, 335.
- (37) Olsson, R. G.; Turkdogan, E. T. *Met. Trans.* **1974**, *5*, 21–26.
- (38) Geurts, F. W. A. H.; Sacco, A., Jr. *Carbon* **1992**, *30*, 415–418.
- (39) Vannice, M. A. *J. Catal.* **1975**, *37*, 449.
- (40) Johnson, A. D.; Daley, S. P.; Utz, A. L.; Ceyer, S. T. *Science* **1992**, *257*, 223.
- (41) Yang, Q. Y.; Maynard, K. J.; Johnson, A. D.; Ceyer, S. T. *J. Chem. Phys.* **1995**, *102*, 7734.
- (42) *Smithells Metals Reference Book*, 6th ed.; Brandes, E. A., Ed.; Butterworth: London, 1983.
- (43) Stafford, S. W.; McLellan, R. B. *Acta Metall.* **1974**, *22*, 1463.
- (44) *Ullmann's Encyclopedia of Industrial Chemistry*; Gerhart, W., Ed., 1985; Vol. A7, p 210.

- (45) Khassin, A. A.; Khanayev, V. M.; Yurieva, T. M.; Kirillov, V. A.; Kulikov, A. V.; Itenberg, I. S.; Parmon, V. N. Fischer–Tropsch Process on Cobalt-Containing Unsupported Catalysts in Slurry Reactor; AIChE Spring National Meeting, 1997, Houston TX.
- (46) Tavares, M. T.; Alstrup, I.; Bernardo, C. A.; Rostrup-Nielsen, J. R. *J. Catal.* **1996**, *158*, 402.
- (47) Jones, F. G.; Pehlke, R. D. *Met. Trans.* **1971**, *2*, 2655.
- (48) Alstrup, I.; Tavares, M. T. *J. Catal.* **1993**, *139*, 513.
- (49) Zaera, F. *Acc. Chem. Res.* **1992**, *25*, 260.
- (50) Trinquier, G.; Hoffman, R. *Organometallics* **1984**, *3*, 370.
- (51) Turner, M. L.; Long, H. C.; Shenton, P. K.; Byers, P. K.; Maitlis, P. M. *Chem. Eur. J.* **1995**, *1*, 549.
- (52) Zaera, F.; Bernstein, N. *J. Am. Chem. Soc.* **1994**, *116*, 4881.
- (53) Borg, H. J.; Martijn van Hardeveld, R.; Niemantsverdriet, J. W. *J. Chem. Soc., Faraday Trans.* **1995**, *91*, 3679.
- (54) Mims, C. A.; Weisel, M. D.; Hoffman, F. M.; Sinfelt, J. H.; White, J. M. *J. Phys. Chem.* **1993**, *97*, 12656.